Published version:

doi.org/10.1016/j.jaerosci.2013.07.005

Two-way coupled numerical simulation of electrospray with induced gas flow

Ajith Kumar Arumugham-Achari [a], Jordi Grifoll [a], Joan Rosell-Llompart [a,b,*]

[a] DEW Laboratory, Chemical Engineering Department, Universitat Rovira i Virgili, 43007 Tarragona, Catalunya, Spain

[b] ICREA (Catalan Institution of Research and Advanced Studies), 08010 Barcelona, Catalunya, Spain

ABSTRACT

The gas flow induced by droplet motion has been included in the numerical simulation of electrosprays. Steady state solutions were sought iteratively in a computational scheme that fully couples a 3D La-grangian model for the droplet dynamics with a steady state 2D axisymmetric Eulerian model for the induced gas flow. To resolve the reactive drag force on the gas by the droplets we employ Gaussian filters with variable kernel widths that depend on the droplet number density. We have applied this scheme to an experimentally characterized spray from the literature comprised of non-evaporating pri-mary and satellite droplets in air. The predicted characteristics of the droplet plume (droplet number density, droplet velocity, droplet size distribution) better match the experimental values when the in-duced airflow is accounted for than when it is not (assuming still air). It is shown that the induced air-flow contributes to faster moving droplets, shrinkage of plume, and a prominent flux about the spray axis (centerline), as compared with the simulations assuming still air. Induced airflow results in an in-crease of 80% in axial droplets velocity at the centerline at the collection counterplate. The ratio of mass flux at the centerline between the cases of moving and still air equals 2.6 at the counterplate. We have also observed that the radial segregation by size of the satellite droplets is sensitive to the functional relationship between their charge-to-mass ratio and diameter. Induced gas flow is expected to have im-portant implications in the simulation of droplet evaporation and vapor concentration in electrosprays.

Keywords: Electrospray, Lagrangian simulation, Induced gas flow, Numerical simulation, Spray dy-namics, Deposition.

Nomenclature

Roman letter symbols

a	factor in the relationship between ξ and d_i (Cm^{-b}/kg,)
b	exponent in the relationship between ξ and d_i
$\mathbf{d}$	ensemble averaged reactive drag force density (N/m^3)
$\mathbf{d}'$	fluctuating component of reactive drag force density (N/m^3)
D_c	capillary tube outer diameter (m)
$\mathbf{D}$	instantaneous reactive drag force density (N/m^3)
C_D	droplet drag coefficient
d_i	diameter of i-th droplet (m)
d_{jet}	electrospray jet diameter (m)
$\bar{d}_p$	count mean primary droplet diameter (m)
$\bar{d}_s$	count mean satellite droplet diameter (m)
$\mathbf{E_{ext}}$	external electrical field (V/m)
$\mathbf{F_i}$	drag force acting on droplet i (N)
$\mathbf{F_i^k}$	drag force acting on droplet i at stage k (N)
$\mathbf{F_{elec,i}}$	electric force acting on droplet i (N)
H	capillary tube tip to counterplate distance (m)
K	Kernel function
K_{Gauss}	Gaussian kernel function
N	number of droplets
n	local ensemble-averaged droplet number density
N_R	number of system realizations for ensemble averaging

p average pressure (Pa)

p' fluctuating pressure (Pa)

P instantaneous pressure (Pa)

q_i electrical charge of droplet i (C)

Q liquid flow rate (m^3/s)

r polar coordinate (m)

Re_i $\left(= \frac{\rho_f |\mathbf{u} - \mathbf{V_i}| d_i}{\mu}\right)$ Reynolds number

$\mathbf{R_i}$ (= $[x_i, y_i, z_i]$) position vector of i-th droplet (m)

$\mathbf{R_i^k}$ position vector of i-th droplet at stage k (m)

$\mathbf{R_I}$ (= $[x_i, y_i, 2H - z_i]$) position vector of image of i-th droplet on counterplate (m)

$\mathbf{R_{ij}}$ (= $\mathbf{R_i} - \mathbf{R_j}$) displacement between the position vectors of droplets i and j (m)

$\mathbf{R_{iJ}}$ (= $\mathbf{R_i} - \mathbf{R_J}$) displacement between the position vectors from the image of droplet j on the counterplate to droplet i (m)

s average separation between the centers of neighboring droplets in the ensemble spray (m)

SD_p Standard deviation of primary droplets' diameters distribution (m)

SD_s Standard deviation of satellite droplets' diameters distribution (m)

$\boldsymbol{t}$ time (s)

$\mathbf{u}$ mean gas velocity vector (m/s)

$\mathbf{u}'$ fluctuating component of gas velocity vector (m/s)

$\mathbf{U}$ instantaneous gas velocity vector (m/s)

V volume of the spray (m^3)

$\mathbf{V_i}$ velocity vector for droplet i (m/s)

V_{jet} electrospray jet velocity (m/s)

$\mathbf{x}$ (=$[x,y,z]$) position vector (m)

z_e	droplet emission point (m)

Greek letter symbols

α	normalization factor
δ	Dirac's delta function
ε_0	electrical permittivity of vacuum (8.854×10^{-12} C/V·m)
ξ	droplet charge to mass ratio (C/kg)
$\overline{\xi}_p$	average charge to mass ratio of primary droplets (C/kg)
$\overline{\xi}_s$	average charge to mass ratio of satellite droplets (C/kg)
$\boldsymbol{\lambda}$	(= $\mathbf{x}$ - $\mathbf{R_i}$) displacement between the position vector $\mathbf{x}$ and position of droplet *i* (m)
μ	dynamic viscosity of surrounding gas (kg/m·s)
ϕ	electrostatic potential (V)
Φ_0	electrostatic potential at the capillary tube (V)
ρ_d	density of drop liquid (kg/m^3)
ρ_f	density of surrounding gas (kg/m^3)
σ	Gaussian kernel width (m)

Acronyms

CFD	Computational Fluid Dynamics
RANS	Reynolds-averaged Navier-Stokes
CVFD	Control Volume Finite Difference
LSC	Lumped Space Charge
OD	Outer diameter

1. Introduction

Electrosprays are dense clouds of highly charged micro drops that are set in motion by the action of external electrostatic fields. Such collections of aerosol particles move with a net velocity relative to the surrounding gas and, as a result, exert a reactive drag force on the gas, which induces gas flow. This gas motion can be significant in the study of electrospray dynamics, particularly when droplet evaporation is involved. Droplet evaporation is a key process for many applications of electrospray, such as electrospray ionization mass spectrometry (ESI-MS) (Fenn et al, 1989; Fenn, 2003), particle synthesis by electrospray (Jaworek & Sobczyk, 2008; Bock et al 2012), and electrospray deposition for the synthesis of thin films and coatings (Jaworek, 2007), in which the extent of droplet evaporation determines whether a film will be granular (Bodnár & Rosell-Llompart, 2013) or display a range of film morphologies (Rietveld et al, 2006).

Because of the difficulty in the experimental accessibility to gas velocity in electrospray systems, only a few experimental reports have addressed the question of gas flow induction by the droplet motion. Tang & Gomez (1994), while carrying out a detailed experimental study on the structure of a heptane electrospray, measured gas velocities along the spray centerline as high as 34% of the droplet axial velocity. Hartman et al. (1999) found that while droplet diameters do not vary radially, their axial velocity dropped as much as 40% from its centerline value. They took this result to mean that the gas must move with a significant axial velocity at the electrospray centerline.

Our ability to predict the induced gas flow pattern is currently very limited because we lack general methodologies for predicting it. The majority of numerical simulation works have assumed the gas to be still as a matter of convenience, given the complexity of the endeavor. The first reported numerical simulation of droplet dynamics in an electrospray is by Gañan-Calvo et al. (1994), who assumed that the surrounding gas is still. The constituent terms of their Lagrangian model are the electrical forces produced by the external field (due to the electrodes) and by the space charge (droplet–droplet Coulombic repulsion, including image charges at the counterplate), and the drag force on the droplets due to friction with the gas. This general model has subsequently been followed to simulate various electrospray systems by different authors, viz., Hartman et al. (1999), Wilhelm et al. (2003), Oh et al. (2008), Jung et al. (2010), Yang et al. (2012) and Grifoll & Rosell-Llompart (2012). The still gas assumption has also been followed in the recent Eulerian model of Higuera (2012).

In some of these works, the assumption of still gas has been justified based on conservation arguments about the global influence of the droplet motion on the gas. Gañan-Calvo et al. (1994) obtained the characteristic droplet velocity by balancing viscous drag to electric force. By globally balancing the energy transferred per unit time to the gas by the spray drag, with the energy dissipated by the viscous stresses outside the spray boundaries, they estimate that the characteristic (average) gas velocity is much smaller than the characteristic droplet velocity. Wilhelm et al. (2003), while evaluating the extent of droplet evaporation, applied global momentum balance to their electrospray system estimate the average gas velocity to be 0.4 m/s, which falls between 3.7% of their highest axial droplet velocity and 11.7% of their lowest one. Higuera (2012) justified neglecting the gas motion in his Eulerian simulation after an order of magnitude estimation of the momentum exchanged between the droplets and the gas.

Since the conservation arguments are based on radially averaged variables, they can overlook regions of high local gas velocity. Therefore, they are not in contradiction with the experimental determinations of high centerline gas velocities which were mentioned earlier. Indeed, using a more detailed approach, Hartman et al. (1999) estimated that the gas velocity close to the spray centerline could be around 32% of droplet axial velocities. They arrived at this conclusion by balancing the electric power of the system with the kinetic power of the induced gas flow (confined within a radius) and the kinetic power of the droplets.

Deng & Gomez (2007) are the first to partially include the effect of gas flow on the droplet drag calculations, by treating the early stage of the spray as a continuous cylindrical surface, and adopting a boundary layer sub-model based on the momentum integral of a logarithmic gas velocity profile.

In sum, while many numerical models have neglected induced gas flow, the experimental evidence shows that the gas speed can be significant locally (at the centerline). Therefore, there is a need for a general methodology to include the induced gas flow caused by the droplets in current numerical models of electrospray dynamics. Furthermore, since the gas motion also influences the droplet motion, a formulation that can *accurately* describe these motions should be *fully coupled* (i.e., *two-way coupled*). Such improved models should be able to elucidate the influence of the induced gas flow on variables of practical importance such as the flux deposition pattern on the counterplate, plume spread, droplet number density distribution, and also in the prediction of droplet evaporation.

In the present work, we have developed a two-way coupled Lagrangian description of the droplet dynamics with an Eulerian description of the induced gas flow. The gas flow description does not consider the detailed flow around each droplet. Instead, two-way coupling is attained by seeking time-averaged pseudo-steady state solutions in both frameworks (droplet dynamics and induced gas flow).

The predictive capability of this methodology is assessed by applying it to the experimentally characterized system of Tang & Gomez (1994) which considers non-evaporating droplets.

2. Methodology

We propose a numerical method that solves for the droplet dynamics and the gas flow using an iterative procedure, and seeks pseudo-steady state solutions using separate codes for the droplet and gas transport equations. The motion of non-coalescent, non-evaporating droplets under electric forces in moving gas is simulated by a 3D Lagrangian particle tracking model. The droplet-induced pseudo-steady gas flow is simulated by a 2D axisymmetric Eulerian model. All of the space within the spray is available to the gas, since the volume fraction of the droplet phase is much smaller than unity (dilute aerosol approximation).

2.1. Governing equations

2.1.1 Lagrangian 'particle dynamics'

The 3D Lagrangian droplet dynamics simulations are based on the model first proposed by Gañán-Calvo et al (1994). The electrospray system is considered to be made of electrostatically interacting droplets considered to be point particles for which the mutual aerodynamic interactions are not considered. The droplets also experience drag from the surrounding gas, and interact with an external electrostatic field created by electrodes (a droplet-emitting capillary tube, and a droplet-collecting plate named *counterplate*). Following these assumptions, the droplet dynamics are described by Newton's second law:

$$\frac{\pi}{6} d_i^3 \rho_d \frac{d\,\mathbf{V_i}}{d\,t} = \mathbf{F_i} + \mathbf{F_{elec,\,i}} \tag{1}$$

where $\mathbf{F_i}$ and $\mathbf{F_{elec,i}}$ are the drag and electric forces acting on droplet *i*, which are given by:

$$\mathbf{F_i} = C_{Di} \frac{\pi}{8} d_i^2 \rho_f (\mathbf{u} - \mathbf{V_i}) |\mathbf{u} - \mathbf{V_i}| \tag{2}$$

where

$$C_{D\,i} = \frac{24}{Re_i}\left(1 + 0.1104\sqrt{Re_i}\right)^2 \tag{3}$$

which is valid for $Re_i < 5000$ (Abraham 1970), and

$$\mathbf{F_{elec,\,i}} = q_i \mathbf{E_{ext}} + \frac{q_i}{4\pi\varepsilon_0} \sum_{\substack{j=1 \\ j\neq i}}^{N} q_j \left(\frac{\mathbf{R_{ij}}}{R_{ij}^3} - \frac{\mathbf{R_{iJ}}}{R_{iJ}^3} \right) \tag{4}$$

The motion of a droplet *i* is described by its position vector $\mathbf{R_i}$ and velocity vector $\mathbf{V_i}$, as

$$\frac{d\,\mathbf{R_i}}{d\,t} = \mathbf{V_i} \tag{5}$$

Equations (1) and (5) are solved for each droplet to obtain its trajectory from the emission point to the counterplate.

2.1.2. Gasflow dynamics and boundary conditions

The body force impelling the gas flow is the reactive drag force due to the droplets' motions. Therefore, the gas motion is governed by the continuity equation (assuming incompressible gas flow) and the Navier-Stokes (momentum transport) equations extended to include droplet drag forces:

$$\nabla \cdot \mathbf{U} = 0 \tag{6}$$

$$\rho_f \left(\frac{\partial \mathbf{U}}{\partial t} + \mathbf{U} \cdot \nabla \mathbf{U} \right) = -\nabla P + \mu \nabla^2 \mathbf{U} + \mathbf{D} \tag{7}$$

where **D** is a fine grained function that describes the reactive drag force per unit volume exerted by the droplets on the gas, which, when droplets are modeled as material points, is given by

$$\mathbf{D}(\mathbf{x}) = \sum_{i=1}^{N} (-\mathbf{F_i})\, \delta(\mathbf{x} - \mathbf{R_i}) \tag{8}$$

The instantaneous flow velocity, pressure and reactive drag force density are split into their time-averaged and fluctuating components as

$$\mathbf{U} = \mathbf{u} + \mathbf{u}' \tag{9}$$

$$P = p + p' \tag{10}$$

$$\mathbf{D} = \mathbf{d} + \mathbf{d}' \tag{11}$$

In the present work, we seek to determine the time-averaged gas flow field $\mathbf{u}$. Hence, Eq. (7) is time-averaged in order to obtain the steady-state fluid flow equation, which is similar to RANS equation in turbulent flows, i.e.

$$\rho_f \mathbf{u}\cdot\nabla\mathbf{u} = -\nabla p + \mu\nabla^2\mathbf{u} - \rho_f \nabla\cdot\left(\overline{\mathbf{u}'\mathbf{u}'}\right) + \mathbf{d} \tag{12}$$

where $\rho_f \overline{\mathbf{u}'\mathbf{u}'}$ is analogous to the Reynolds stress term in turbulent flow, though different in its cause. In order to account for this viscous-like stress in Eq. (12), a closure model would be needed. This closure model could be formulated either by comparing system-specific solutions of Eqs. (6-7), or detailed experimental data, to Eq. (12). Here, the gas velocity perturbations $\mathbf{u}'$ are associated with the local perturbations on the gas mean flow caused by passing droplets. Therefore, such system-specific solutions or data would have to resolve very fine flow scales, and thus present enormous difficulties. Any such approach is beyond the scope of the present formulation, in which, as a first approximation, the term $\rho_f \nabla\cdot\left(\overline{\mathbf{u}'\mathbf{u}'}\right)$ is neglected.

The computational domain and boundary conditions for the gas flow are 2D axisymmetric, as shown in Fig. 1. The surfaces of the cylindrical capillary tube electrode and the counterplate are assumed to be stationary walls with no-slip conditions imposed on them. The gas is free to flow in and out through the open boundaries, in such a way that the flow is normal at the top boundary and fulfills a self similarity condition at the side boundary (Deshpande & Vaishnav, 1982). The jet extends from below the capillary tube (Fig. 1), and moves with velocity V_{jet} which is estimated from the total flow rate and d_{jet} by the mass conservation principle ($=4Q/\left(\pi d_{jet}^2\right)$). The surface of the electrospray jet is modeled as a cylindrical boundary of uniform diameter d_{jet}, which can be estimated from the count mean droplet diameter as $\bar{d}_p$/1.89 (Tang & Gomez, 1994; Rosell-Llompart & Fernandez de la Mora, 1994).

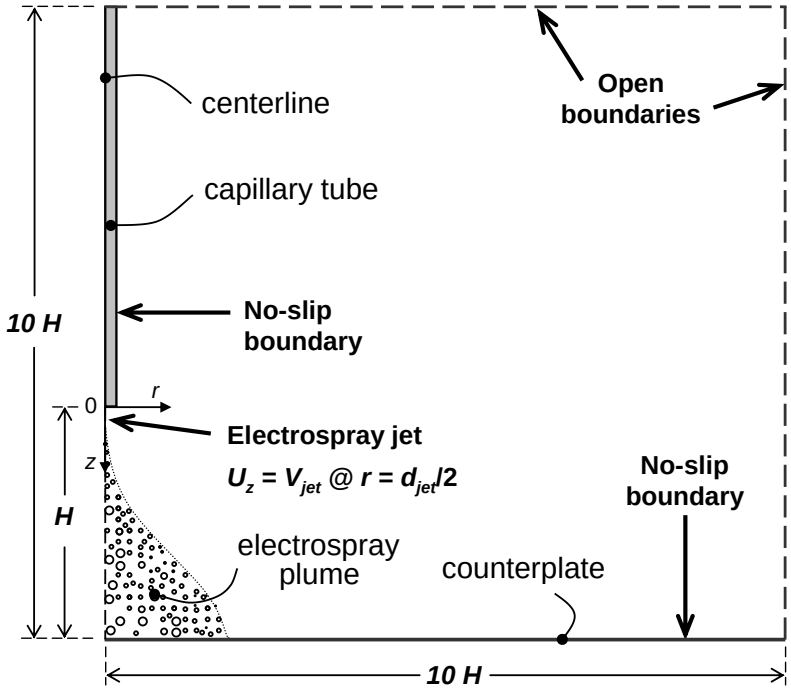

Fig. 1. Schematic diagram of the 2D axisymmetric computational domain for the gas flow, including boundary conditions.

2.1.3. Ensemble averaged reactive drag force

In Eq. (12) the reactive drag force density **d** can be computed by ensemble averaging Eq. (8) over a large number N_R of system realizations (ergodic hypothesis). N_R is defined as "large" enough to make **d** become independent of N_R. In addition, the fine grained (singular) description based on Dirac's delta must be replaced with a coarser grained (non-singular) kernel function K such that

$$\mathbf{d}(\mathbf{x}) = \frac{1}{N_R}\sum_{k=1}^{N_R}\sum_{i=1}^{N}\left(-\mathbf{F}_\mathbf{i}^\mathbf{k}\right)K\left(\mathbf{x}-\mathbf{R}_\mathbf{i}^\mathbf{k}\right) \tag{13}$$

In this work we employ the *Gaussian kernel* defined as

$$K_{Gauss}(\boldsymbol{\lambda}) = \alpha\,\frac{\exp\left[-|\boldsymbol{\lambda}|^2/(2\sigma^2)\right]}{\sigma^3} \tag{14}$$

where σ is the filter width for smoothing the reactive drag forces, and α is a normalization factor that ensures conservation of force globally within the ensemble averaged system, so that

$$\sum_{k=1}^{N_R}\sum_{i=1}^{N}\left(-\mathbf{F}_\mathbf{i}^\mathbf{k}\right) = N_R \int_{\substack{\text{spray}\\ \text{volume}}} \mathbf{d}(\mathbf{x})\, dV \quad . \tag{15}$$

Similar smoothing of the particle drag force has been employed in numerical simulations of particle laden flows (Kitagawa et al, 2001; Maxey & Patel, 2001; Apte et al, 2008; Finn et al, 2011).

Deen et al. (2004) suggest that the filter width should be in the order of particle diameter, rather than at finer length scales. This is a logical consequence of the fact that each droplet transfers its drag to the gas phase at the droplet surface. Kim et al. (1993) simulated three-dimensional flow over two fixed spheres normal to the line connecting their centers, for $50 < Re < 150$. They found that the drag increases as the spheres become close together, and that the drag coefficient for separations larger than four diameters differs by less than 0.7% of the drag for an isolated single sphere. Since the kernel width should not be smaller than the "region of influence" of the drag force, the smallest kernel width extends to about two droplet diameters in this study.

At the same time, our formulation is tolerant of filter widths that are larger than the particle diameter, as long as $\mathbf{d}(x, y, z)$ remains unchanged. This can happen when σ is sufficiently smaller than the characteristic distance for maximum change of $\mathbf{d}$:

$$\sigma << \frac{|\mathbf{d}|}{|\nabla \mathbf{d}|_{\max}} \tag{16}$$

Finally note that any choice of filter width σ implies a large enough ensemble (large enough N_R), such that the density force field becomes independent of the ensemble size. In other words, the graininess of the ensemble spray should not be "imprinted" onto $\mathbf{d}(x, y, z)$, which, instead, should be a smooth function of position. In mathematical terms, in the ensemble spray the droplet centers must be much closer together than the filter width σ:

$$\sigma >> s \equiv \left(nN_R\right)^{-1/3},$$

where n is the local ensemble-averaged droplet number density, and s is the average separation between the centers of neighboring droplets in the ensemble spray. Therefore N_R must fulfill:

$$N_R >> \frac{1}{n\sigma^3} \tag{17}$$

2.2. Numerical implementation

The numerical scheme has been implemented in three parts: droplet dynamics, reactive drag force calculation, and gas flow dynamics. These parts have been run iteratively through successive stages according to the flow chart shown in Fig. 2. Initially (stage 0), quiescent gas is assumed ($\mathbf{u} = 0$) and the droplet dynamics is simulated long enough to ensure that a statistically significant portion of the steady state is captured (Grifoll & Rosell-Llompart, 2012). Using this solution, an ensemble-averaged drag force field is computed. Such field is then used with the gas dynamics code to compute the steady-state velocity field solution. This solution is then fed back into the droplet dynamics simulation, initiating a new stage of the global iteration loop. The overall scheme is considered to have converged by comparing the gas flow solutions of two consecutive stages. A more detailed description of these steps is provided next.

2.2.1. Droplet dynamics and the reactive drag force calculation

The present 3D Lagrangian droplet dynamics simulations use the LSC method of Grifoll & Rosell-Llompart (2012). This scheme simplifies the far droplet-droplet electrostatic interactions (last term of Eq. (4)) using a coarse-graining approximation without any significant loss in accuracy.

Upon attaining a droplet dynamics solution, the droplets' relative velocities $\mathbf{(V_i - u)}$ and position data $\mathbf{R_i}$ are used to compute the corresponding drag forces $\mathbf{F_i}$ (Eq. (2)). Next, through the methodology explained in *Section 2.1.3*, the fine grained reactive drag force data are ensemble averaged over N_R realizations. Then, they are smoothed in a 3D Cartesian grid of cubic elements of side equal to the kernel width. And these smoothed data are then transformed from the 3D Cartesian domain to the 2D cylindrical domain in which the computation of gas flow is carried out (Fig. 1).

2.2.2. Gas flow dynamics

The 2D Eulerian gas flow computations are based on the stream function-vorticity formulation and on the Control Volume Finite Difference (CVFD) discretization scheme proposed by Gosman et al. (1969). The CVFD methodology is an integral approach which considers control volumes, each surrounding a computational node. It has the advantages of ensuring the conservation laws and ease of physical interpretation and implementation. More details of this discretization scheme and the solution procedure can be found in Deshpande & Vaishnav (1982). The numerical scheme was tested against the laminar jet

problem of Deshpande & Vaishnav (1982), resulting in better than 2% agreement in the stream function values.

At each iteration stage (Fig. 2), the computed gas flow field is fed to the droplets dynamics code in order to update the spray configuration. The drag forces on the droplets are re-calculated according to Eq. (2) where the updated gas velocity at the droplets positions is interpolated from its values at the neighboring grid points. Since the variation in velocities between contiguous grid points is small, we opt for zero-order interpolation, namely taking the gas velocity value of the cell to which each droplet belongs.

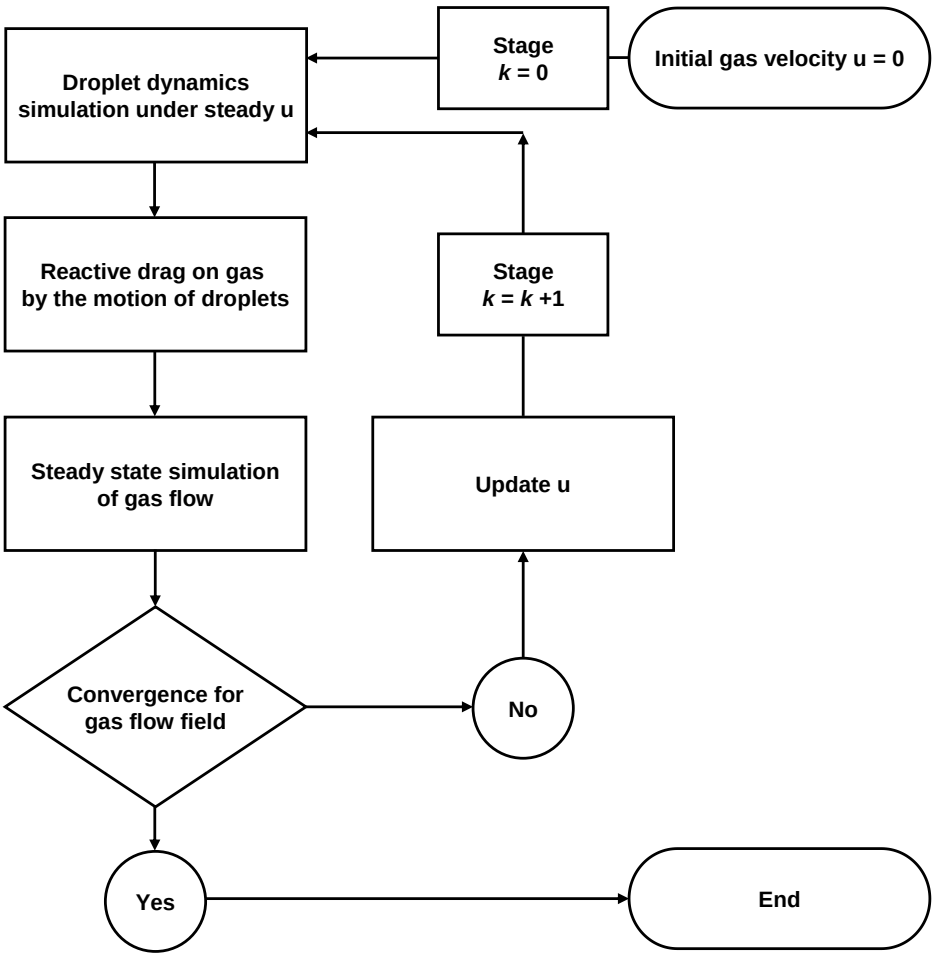

Fig. 2. Numerical scheme for two-way coupling.

3. Results and discussion

3.1. System description

The numerical scheme has been applied to simulate the experimental system of Tang & Gomez (1994), whose parameters are provided in Table 1. This system was previously simulated under the assumption of still air by Grifoll & Rosell-Llompart (2012).

This spray is comprised of non-evaporating primary and satellite droplets. The primary droplet size distribution is the experimental histogram provided by Tang & Gomez (1994), while the satellite droplet distribution is assumed to be log-normal, also based on their data. The computation for droplet charge (q) for both primary and satellite droplets is based on a single functional dependence of charge-to-mass ratio (ξ) with droplet diameter (d):

$$\xi = ad^b \tag{18}$$

Details on the goodness of the two parameters a and b can be found in Gamero-Castano (2008) and Hai-Bin Tang et al. (2011). For the present spray configuration these parameters were calculated to be $a = 6.13\times10^{-9}$ Cm$^{1.5}$/kg and $b = -1.5$. These values are chosen to be consistent with the report of Tang & Gomez (1994), who find an average charge density of the primary droplets equal to 22.5 C/m^3, and a charge-to-mass ratio dependence with the average diameters for the primary and the satellite droplets given by:

$$\frac{\bar{\xi}_p}{\bar{\xi}_s} = \left(\frac{\bar{d}_p}{\bar{d}_s}\right)^{-1.5} \tag{19}$$

The external electrical field has been calculated by solving Laplace's equation for the electrostatic potential ϕ in the region between the capillary tube and the counterplate, in cylindrical coordinates, using a very fine non-homogeneous grid. The boundary conditions are $\phi = \Phi_0$ at the capillary tube and Taylor cone surfaces; $\phi = 0$ V at the plate, $\partial\phi/\partial z = 0$ at $z = -9H$, and $\partial\phi/\partial r = 0$ at $r = 10H$.

Taking the largest droplet velocity in the system as equal to the jet velocity, we can estimate an upper bound of the Reynolds number, which is 27 for an average droplet moving in still air. This value is well within the range of application of Eq. (3).

Table 1. System configuration*

Parameter (units)	Sym-bol	Value
Capillary-to-plate separation (m)	H	0.03
Capillary tube OD (μm)	D_c	450
Droplet emission point (cm)	z_e	0.24
Count mean diameter for primary droplets (μm)	$\bar{d}_p$	32.3
Coefficient of variation of primary droplets' diameter	$SD_p/\bar{d}_p$	0.06
Count mean diameter for satellite droplets (μm)	$\bar{d}_s$	9.96
Coefficient of variation of satellite droplets' diameter	$SD_s/\bar{d}_s$	0.25
Capillary potential (V)	Φ_0	5000
Liquid flow rate (cc/h)	Q	10

*From Tang & Gomez (1994)

3.2. Selection of kernel width

Finding the steady state solution to the governing equations requires a smooth reactive drag force field, since the streamfunction-vorticity formulation uses the spatial derivatives of such force field. Initially we tried computing the reactive drag force density by simply averaging the contributions from droplets present within given control volumes. However, the number of system realizations needed to get a smooth force field became prohibitive. Instead, we have tested the effect of various Gaussian kernel widths (σ) on the smoothing of the ensemble averaged reactive drag force (**d**), as explained in *Section 2.1.3.* We have found that 3000 is a practical number of system realizations (N_R) in this system. Such realizations (independent snapshots) were selected at equally spaced times within the period $0.1 < t < 0.7$ s, in which the system was found to be under steady state (following the criterion of Grifoll & Rosell-Llompart, 2012).

Fig. 3 shows the effect of the Gaussian kernel width (σ) on the axial component of the reactive force density along the centerline. These curves are smooth near the droplet emission point between z_e (0.24 cm) and several mm downstream. But they display increasing noisiness further downstream. This noise grows in amplitude for the smaller values of σ, and is due to statistical under-sampling in regions of the spray where the number density is so low that Eq. (17) is not fulfilled. In the emission point region, the different curves do not coincide, nor do they show an asymptotic trend. This effect is due to the use of kernel sizes which are wider than the spray in this region (shown later). Indeed, near to the emission

point the swarm of droplet centers cluster tightly together around the centerline, within a radius that is smaller than the average primary droplet diameter ($\bar{d}_p$). A choice of kernel width much smaller than $\bar{d}_p$ would lead to an asymptotic **d**(x, y, z) function, provided N_R was large enough. However, such **d** would have no physical meaning because the drag force is transferred from the droplet phase to the gas phase at the length scale defined by the radius of the droplet-air interface (droplet radius) rather than at significantly finer scales.

In order to avoid the large fluctuations found in some of the force density curves of Fig. 3, we have used a combination of kernels in different regions, as summarized in Table 2. In the region near the emission point we have chosen a kernel width of approximately 2 primary mean droplet diameters (σ = 75 μm) (*Section 2.1.3*). In regions far away from the emission point, where the spray becomes more dilute, the kernel widths have been increased as given in Table 2.

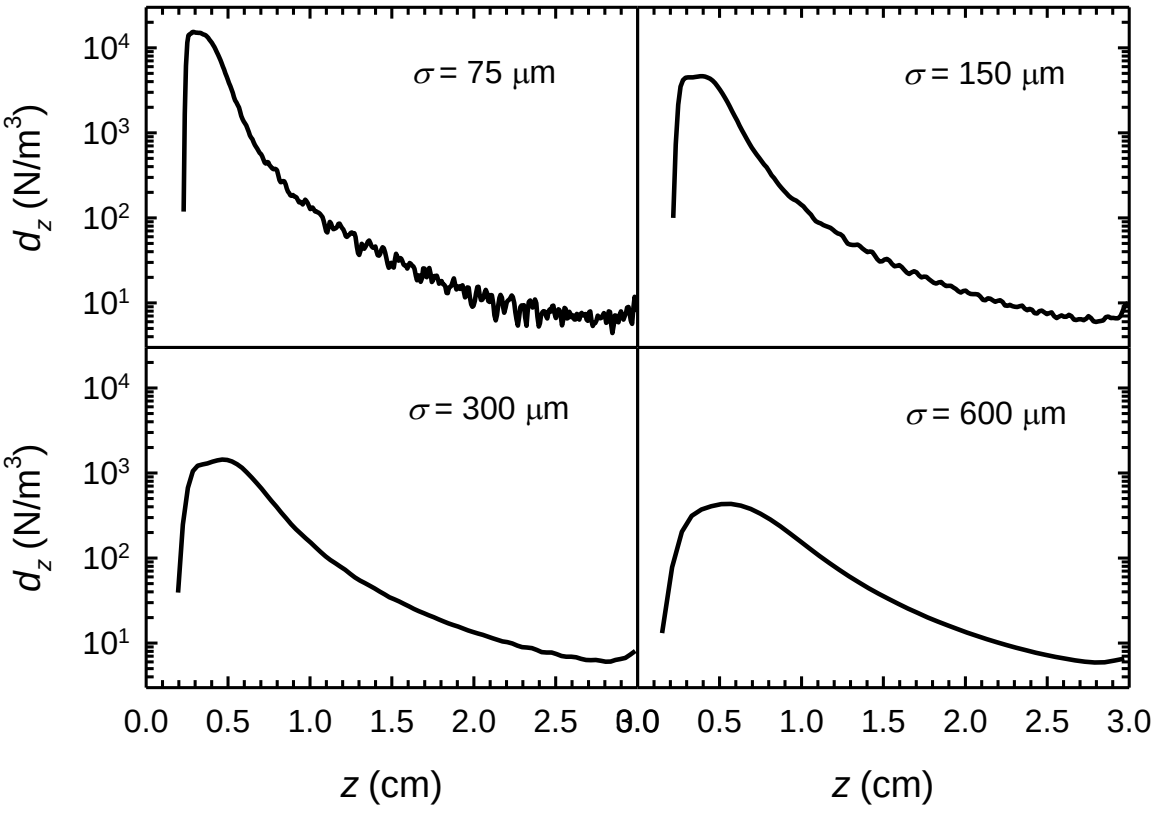

Fig. 3. Reactive drag force computed along the axis for different kernel widths.

Table 2. Characteristics of the tested kernels.

Kernel size, σ (μm)	Axial range of use (cm)
75	0.0 – 0.6
150	0.6 – 1.0
300	1.0 – 1.5
600	1.5 – 3.0

3.3. System simulation

The streamlines for steady-state induced air flow on attaining convergence after five global iterations are shown in Fig. 4a, superimposed on a snapshot of the simulated spray system, also in steady state. Figure 4b shows another snapshot of the same system, however obtained assuming still air. In both of these simulations the model predicts the segregation of droplets experimentally observed by Tang & Gomez (1994), whereby a shroud of satellite droplets forms around a core of primary droplets. The airflow streamlines of Fig. 4a show the formation of a jet-like structure. The flow impinges onto the counterplate wherefrom it develops a wall jet boundary layer.

These airflow computations were performed using a non-uniform grid of 193×252 cells extending 10H×10H (Fig. 1). The smallest radial grid size corresponds to $d_{jet}/2$ at the centerline, whereas the smallest axial grid size is 45 μm both at the counterplate and at the capillary tube tip. Grid independency was tested using a double refined grid (386×504 cells). The maximum difference in velocity field between the two solutions was found to be 5.7% at the axis (z = 0.25 cm), and the average variation was 0.12% for the entire flow domain.

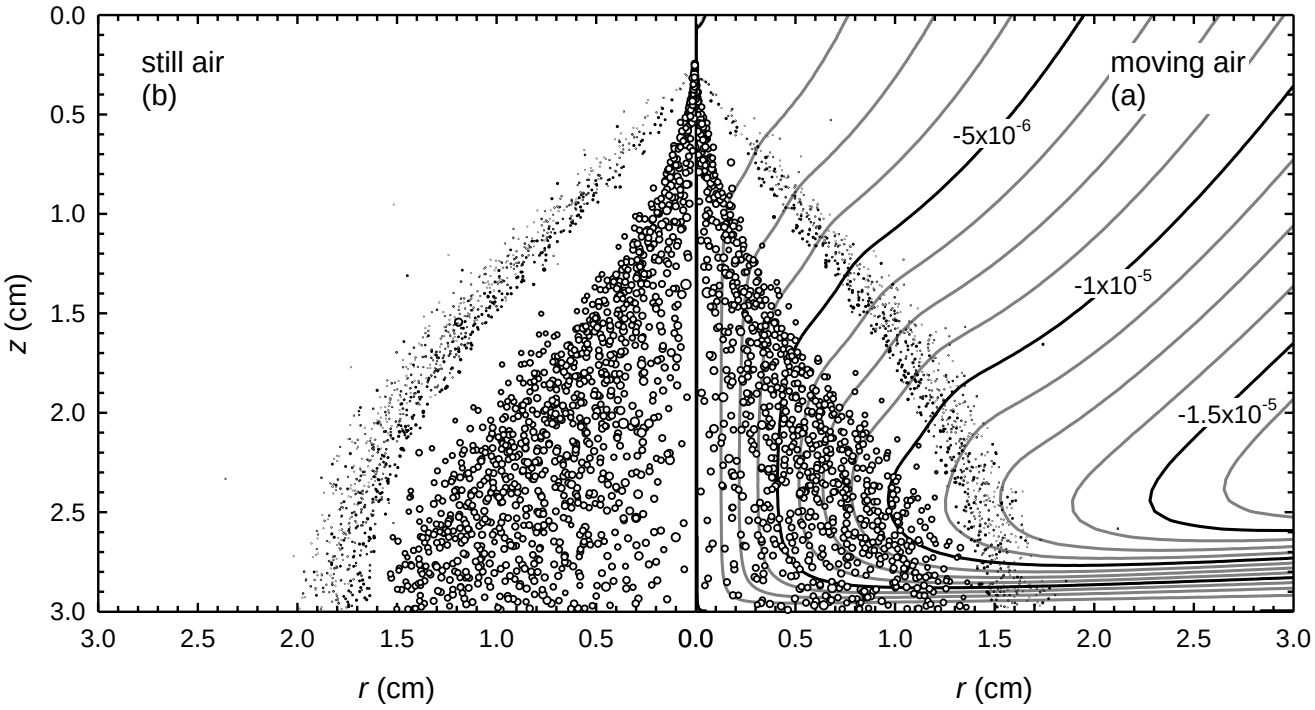

Fig. 4. Spray snapshots projected on *rz* plane for (a) simulation with moving air, including the streamlines of the induced air flow, and (b) simulation with still air. The circles diameters are proportional to the actual droplet diameters.

The radial profiles of the axial and radial air velocity components (Figs. 5a, b) show that high air velocities occur mainly in a region close to the spray axis. Fig. 5a shows that the axial velocity attains its maximum value at the axis near the emission point. At all axial positions, the axial velocity decays radially from a maximum value at the axis, and is below 0.1 m/s for $r > 0.8$ cm. The inward (negative) radial velocity found at $z = 0.5$ and 1.5 cm (Fig. 5b) is due to the air entrainment effect (see Fig. 4). When the counterplate is approached (curve for $z = 2.5$ cm) the radial velocity increases as the air spreads radially out forming a wall jet like pattern. The humps present in all these velocity profiles correlate to the presence of the primary and satellite droplet plumes.

The observed radial drop in axial velocity shown in Fig. 5a is consistent both with the previous experimental determinations of centerline air velocities, and with the conclusions from various radially-averaged conservation balances, that were mentioned earlier in the Introduction.

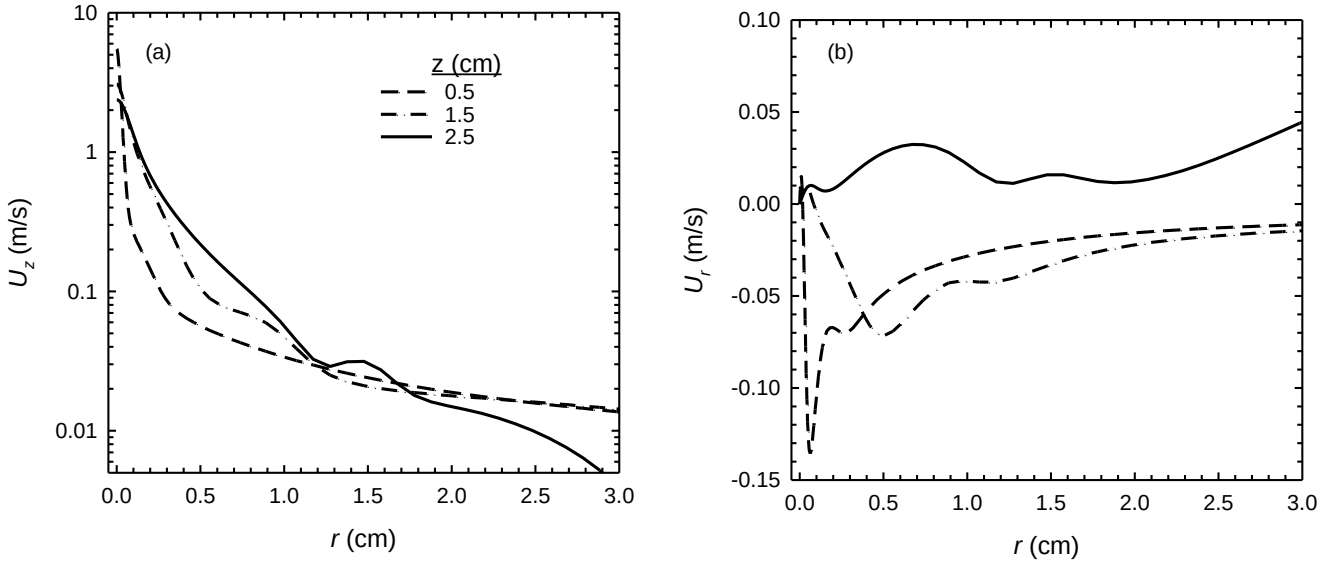

Fig. 5. Air velocity at various axial positions: (a) axial component, (b) radial component.

Fig. 6 graphs the centerline velocity of the air and the droplets obtained in the experiments of Tang & Gomez (1994) and in the present simulations with and without air flow. Droplets velocities simulated when the air is at rest (gray line) significantly underpredict the experimental values. This line displays a monotonous decrease in the *initial spray zone* ($z < 0.8$ cm), unlike the experimental data (squares). On the other hand, the simulations that account for airflow predict air and droplet velocities which are in fair agreement with the experimental data. In the *downstream spray zone* ($z > 0.8$ cm), the simulated air velocity (dashed line) decays slower than the experimental data (circles), overpredicting them.

We should note that had we computed the air velocity fluctuations term $\rho_f \nabla \cdot \left(\overline{\mathbf{u}'\mathbf{u}'}\right)$ in Eq. (12), a faster decay of the axial air velocity would have been obtained, because this term would enhance the momentum transfer. In numerical simulations of *electric wind* caused by corona discharges by Zhao & Adamiak (2005) this term was also neglected, and a similar overprediction of the axial air velocities was found, with an increasing deviation towards the centerline. Since the radial variation of axial velocity is maximum at the centerline, this is where maximum overprediction of gas velocity would be expected.

To better understand the droplet dynamics along the centerline, it is also helpful to look at the different terms of the droplet momentum equation (Eq. (1)): the inertia term, the drag force, and the electrical force. We have taken all 3000 snapshots and have averaged each of these terms within equal cylindrical slices of radius 0.03 cm centered at the centerline. As shown in Fig. 7, the drag tends to zero at the

emission point because the droplet and air velocities are equal (to the jet velocity, 12.3 m/s). (This behavior is opposite to the case of still air, for which the drag is *maximum* at this position, rather than *minimum*, and the droplet velocity decays with a significant slope; as shown by the grey line in Fig. 6.) Initially (near the droplet emission point), the air momentum at the centerline is rapidly transferred to its surroundings due to the action of viscous stresses, causing a rapid drop in air velocity at the centerline (Fig. 6). As a result, the drag force on the droplets (Fig. 7) suddenly increases; however this change is too short lived to appreciably change the droplet velocity (Fig. 6). Beyond this initial transition, which ends at about $z = 0.4$ cm, the air slows down at a much slower rate. Up to this location the inertia term is near zero (Fig. 7), consistently with a nearly constant droplet velocity in both the simulated and the experimental results (Fig. 6). Beyond this zone ($z > 0.4$ cm), the air velocity continues to decrease (Fig. 6), causing an increase in the drag force (Fig. 7), and the electrical force starts to decrease. At about $z = 0.55$ cm, the drag force reaches a maximum when both the droplets and the air slow down at equal rates. Near the counterplate, the air stream is deflected and the axial velocity drops towards zero (Fig. 6). As a result, the drag force on the droplets is increased (Fig. 7), though with minimal effect on the droplet velocity (Fig. 6). These simulations also show that along the axis the droplets do not attain electrophoretic motion (zero inertia).

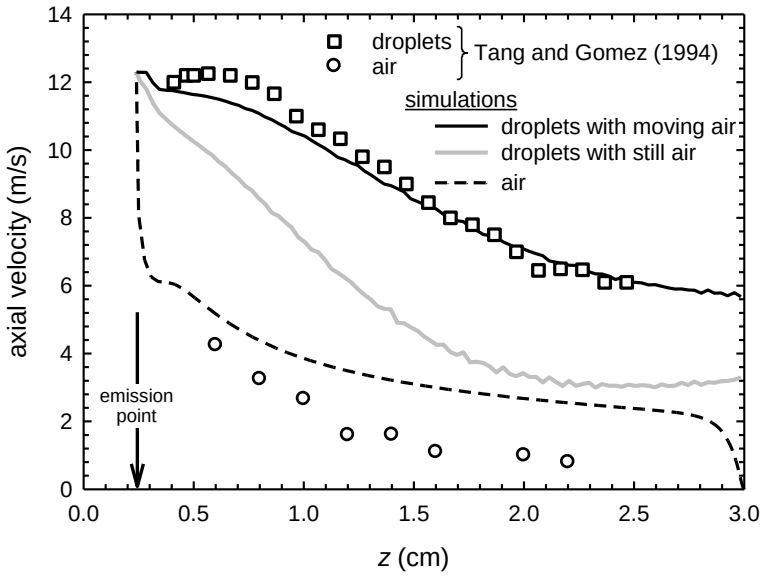

Fig. 6. Numerical and experimental values of axial velocities along the centerline for air and droplets.

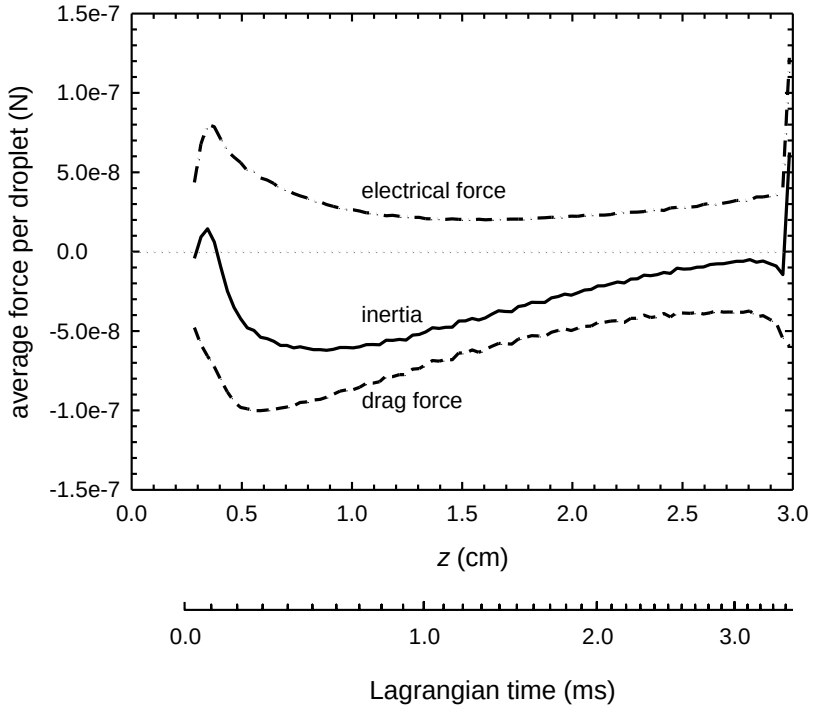

Fig. 7. Average electrical forces, drag forces, and inertia sensed by the droplets along the centerline. Secondary abscissa shows the droplet Lagrangian time based on the droplet axial velocity given in Fig. 6.

Tang & Gomez (1994) also show radial distributions of the number density and average droplet diameter at a constant axial position of z = 1.2 cm. In Fig. 8 we compare these data to our numerical predictions with and without airflow. Volumetric bins of height 250 μm, consistent with the kernel size at this axial location (z = 1.2 cm) were considered for these calculations.

The number density distribution (Fig. 8a) shows a similar pattern to the experimental data, with a core spray of primary droplets, surrounded by a shroud of satellite droplets. Only when the model includes airflow, the number density near the centerline increases to a maximum, in qualitative agreement with the experimental data. However, a disagreement in number density is found close to the axis, within a region of radius ~1 mm. This disagreement could be the result of two causes. First, the actual charge-to-mass ratio for the largest droplets might be higher than as defined in Eq. (19). If so, the actual particles would be expected to expand radially faster than predicted by the present model, leading to a reduced number density. Second, because the model neglects the fluctuation term $\rho_f \nabla \cdot \left(\overline{\mathbf{u}'\mathbf{u}'} \right)$ (as discussed earlier), it may lead to overprediction of the air axial velocity at the centerline, resulting in a

shorter Lagrangian time for the droplets. This would imply lesser expansion by space charge repulsion near the centerline, and an increased number density.

We have quantified the effect on the number density shown in Fig. 8a when increasing the kernel size in the initial axial range, $0 < z < 0.6$ cm (Table 2) from 75 to 150 μm. The effect is minor, with only a 7% decrease in the number density at the centerline ($r = 0$) which rapidly diminishes to a 1.4% decrease at $r = 0.5$ mm. However, as argued earlier in the context of Fig. 3, 75 μm is a more appropriate kernel size for the initial axial range.

On the other hand, the locations of both the primary and satellite droplet plumes show better agreement with the experiments, than the simulations which consider still air. This improvement is the result of two factors. First, the axial motion of the cloud is faster in the presence of airflow. Therefore, the droplets sampled at a fixed z are "younger" (in Lagrangian time) than when airflow is neglected. And a younger spray should have expanded radially less than an older one. Second, the radially converging airflow close to the droplets' emission point reduces the extent of radial expansion (Fig. 4).

The average diameter profile (Fig. 8b) also shows better overall agreement with the experimental data when airflow is included than when it is not (except in regions for which the droplet count, shown in Fig. 8a, is very low).

Initially, we had carried out the simulations assuming a constant charge-to-mass ratio for both primaries and satellite droplets, as done previously by Grifoll & Rosell-Llompart (2012) in absence of airflow. This assumption was consistent with the information provided in Tang & Gomez (1994), but, under the presence of airflow, resulted in *reverse* dependence of local satellite diameter *versus* r. In conclusion, the radial segregation by size of the satellite droplets is sensitive to the functional relationship between charge-to-mass ratio and diameter. By contrast, the assumed relationship given by Eq. (18), which is also consistent with Tang & Gomez (1994), leads to a correct prediction of the segregation effect (Fig. 8b).

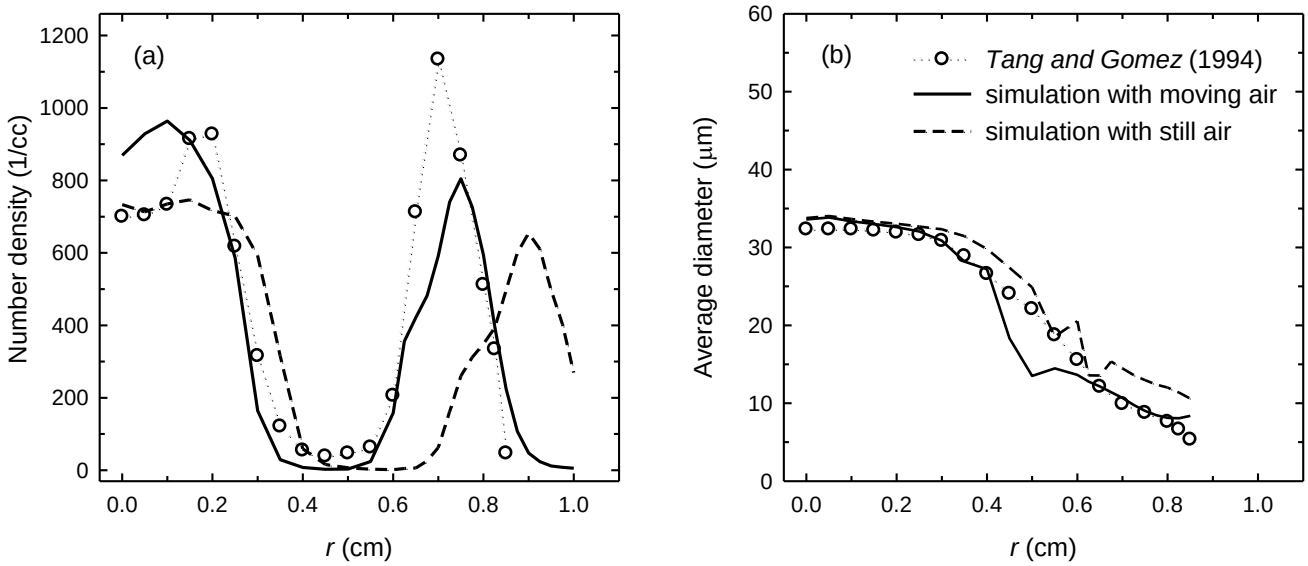

Fig. 8. Radial profiles at z =1.2 cm of (a) droplet number density, and of (b) droplet diameter.

Figs. 9a, b show the radial distributions of the droplets' axial mass flux at two axial locations (z = 1.2 cm and on the counterplate, i.e. z = 3 cm) for the cases of still air and moving air. The ability to predict the droplet mass flux is of interest to practitioners of electrospray deposition who make thin films and coatings. In Figs. 9a and b, the contribution from the satellite droplets to the mass flux is extremely small, as can be confirmed by comparing Fig. 9a with Fig. 8a, and 9b with 4 . The effect of the induced airflow is to raise the mass flux near the center and reduce the plume width. The ratio of mass flux at the centerline between the cases of moving and still air is 2.2 at z = 1.2 cm, and 2.6 at z = 3.0 cm. This effect is the result of the aforementioned causes of inwardly radial airflow and reduction of Lagrangian time available for cloud expansion. An indication of reduced residence time of the plume in the presence of airflow is the reduction in average number of primary droplets in the plume from 1125 in still air to 904 in moving air, and in the average number of satellites from 1755 to 1656. It should be noted that close to the centerline, the flux may be overpredicted since, while the droplet velocity closely agrees with the experiments (Fig. 6), the centerline number density is overpredicted (Fig. 8a).

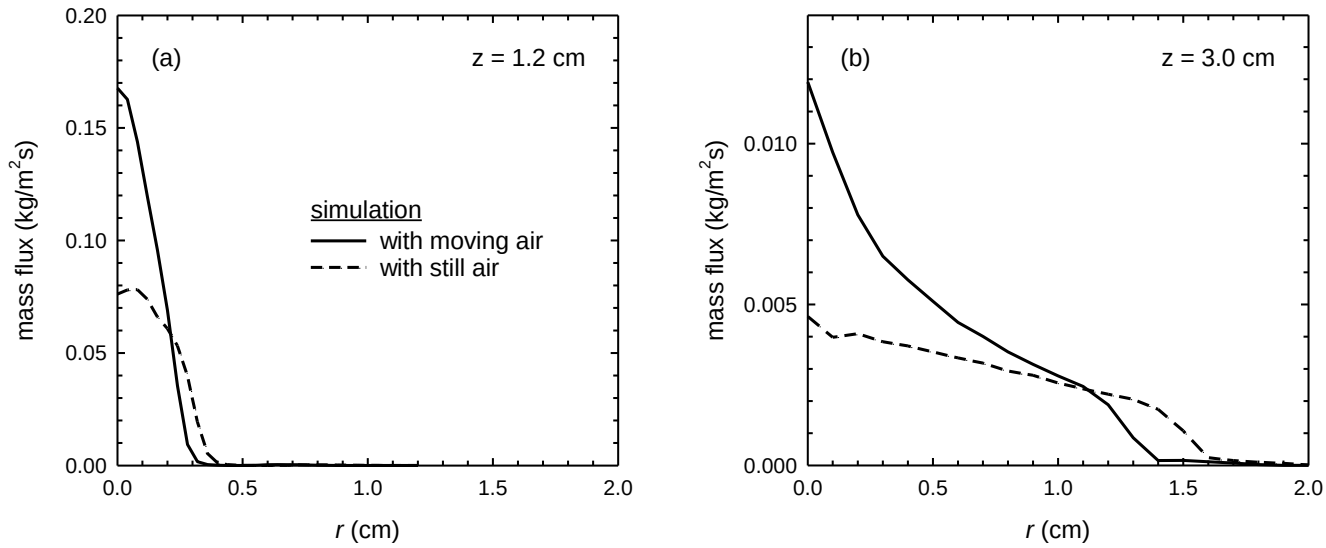

Fig. 9. Comparison of mass flux assuming still or moving air at (a) z = 1.2 cm and (b) z = 3.0 cm.

4. Conclusions

The air flow induced by droplet motion has been included into a Lagrangian model of electrosprays. Steady state solutions for air flow and droplet dynamics were sought iteratively in a fully coupled computational scheme. Detailed simulations have been performed on an electrospray plume which was experimentally characterized by Tang & Gomez (1994). Results show that including air motion in the simulations modifies the droplet trajectories significantly. Radial profiles of number density, and of local average droplet diameter, and centerline droplet velocities show better agreement with the experimental data when airflow is taken into account. Significant air entrainment towards the spray axis is observed near the droplet generation region, which develops into a jet like structure that impinges onto the counterplate. The droplets mass flux radial distribution is particularly sensitive to the air entrainment, which results in a steep increase near the spray axis.

In order to resolve the reactive force on the air by the droplets while using a practical number of independent system realizations, it is necessary to use a filter. In the present simulations, with 3000 ensemble-averaged realizations, we have used a range of Gaussian filters differing in kernel width at different axial locations. At the denser spray regions close to the droplet emission point, the kernel size should neither be much wider nor much smaller than the average droplet diameter. Further downstream,

where the droplet number density decreases, a wider kernel width has been used in order to suppress the fluctuations in the reactive force density.

Acknowledgments

The research was financially supported by the Spanish Government (grants CTQ2008-05758/PPQ and DPI2012-35687), and by the Generalitat de Catalunya (grant 2009SGR-01529). A.K.A. acknowledges a scholarship granted by the Universitat Rovira i Virgili.

References

Abraham, F. F. (1970). Functional dependence of drag coefficient of a sphere on Reynolds number. *Physics of Fluids, 13,* 2194-2195.

Apte, S.V., Mahesh, K., & Lundgren, T. (2008). Accounting for finite-size effects in simulations of disperse particle-laden flows, *Int. J. Multiphase Flow, 34,* 260-271.

Bock, N., Dargaville, T.R., Woodruff, M.A. (2012). Electrospraying of polymers with therapeutic molecules: State of the art, *Progress in Polymer Science, 37,* 1510-1551.

Bodnár, E. & Rosell-Llompart, J. (2013). Growth dynamics of granular films produced by electrospray, *J. Coll. Int. Sci.*, submitted.

Deen, N.G., van Sint Annaland, M., Kuipers, J. A. M. (2004). Multi-scale modeling of dispersed gas-liquid two-phase flow. *Chem. Eng. Sci., 5*9, 1853-1861.

Deng, W., & Gomez, A. (2007). Influence of space charge on the scale-up of multiplexed electrosprays. *J. Aeros. Sci., 38,* 1062-1078.

Deshpande, M.D., & Vaishnav, R.N. (1982). Submerged laminar jet impingement on a plane. *J. Fluid Mech., 114,* 213-236.

Fenn, J.B., Mann, M., Meng, C.K., Wong, S.F., & Whitehouse, C.M. (1989). Electrospray ionization for mass spectrometry of large biomolecules, *Science, 246* (4926), 64-71.

Fenn, J. B. (2003). Electrospray wings for molecular elephants (Nobel lecture), *Angew. Chem.-Int. Ed., 42*(33): 3871-3894.

Finn, J., Shams, E., & Apte, S. V. (2011). Modeling and simulation of multiple bubble entrainment and interactions with two dimensional vortical flows. *Phys. Fluids, 23*, 023301 (1-20).

Gamero-Castano, M. (2008). The structure of electrospray beams in vacuum. *J. Fluid Mech., 604*, 339-368.

Gañan-Calvo, A. M., Lasheras, J.C., Davila, J., & Barrero, A. (1994). The electrostatic spray emitted from an electrified conical meniscus. *J. Aeros. Sci., 25*, 1121-1142.

Gosman, A. D., Pun, W. M., Runchal, A. K., Spalding, D. B., & Wolfshtein, M. (1969). *Heat and mass transfer in recirculating flows*. Academic Press Inc.: London.

Grifoll, J. & Rosell-Llompart, J. (2012). Efficient Lagrangian simulation of electrospray droplets dynamics. *J. Aeros. Sci., 47*, 78-93.

Hai-Bin Tang, Chao-Jin Qin & Yu Liu. (2011). Characterization of colloid thruster beams and plumes. *J. Aeros. Sci., 42*, 114-126.

Hartman, R. P. A., Borra, J. P. , Brunner, D. J. , Marijnissen, J. C. M., & Scarlett, B. (1999). The evolution of electrohydrodynamic sprays produced in the cone-jet mode, a physical model. *J. Electrostat., 47*, 143-170.

Higuera, F. J. (2012). Eulerian model of a dilute spray of charged droplets. *J. Aeros. Sci., 48*, 34-45.

Jaworek, A. (2007). Electrospray droplet sources for thin film deposition. *J. Mater. Sci., 42*, 266-297.

Jaworek, A. & Sobczyk, A.T. (2008). Electrospraying route to nanotechnology: An overview. *J. Electrostat., 66*, 197-219.

Jung, J. H., Oh, H., & Kim, S. S. (2010). Numerical simulation of the deposition pattern in multiple electrohydrodynamic spraying. *Powder Technol., 198*, 439-444.

Kim, I., Elghobashi, S., Sirignano, W. A. (1993) Three-dimensional flow over two spheres placed side by side. *J. Fluid Mech., 246*, 465-488.

Kitagawa, A., Murai, Y., Yamamoto, F. (2001). Two-way coupling of Eulerian–Lagrangian model for dispersed multiphase flows using filtering functions. *Int. J. Multiphase Flow, 27*, 2129-2153.

Maxey, M.R., & Patel, B.K. (2001). Localized force representations for particles sedimenting in Stokes flow. *Int. J. Multiphase Flow, 27*, 1603-1626.

Oh, H., Kim, K., & Kim, S. (2008). Characterization of deposition patterns produced by twin-nozzle electrospray. *J. Aeros. Sci., 39,* 801-813.

Rietveld, I. B., Kobayashi, K., Yamada H., & Matsushige, K. (2006). Electrospray deposition, model, and experiment: Toward general control of film morphology. *J. Phys. Chem. B, 110,* 23351-23364.

Rosell-Llompart, J. & Fernandez de la Mora., J. (1994). Generation of monodisperse droplets 0.3 to 4 μm in diameter from electrified cone-jets of highly conducting and viscous liquids. *J. Aeros. Sci., 25,* 1093-1119.

Tang, K. & Gomez, A. (1994). On the structure of an electrostatic spray of monodisperse droplets. *Phys. Fluids, 6,* 2317-2332.

Wilhelm, O., Madler, L., & Pratsinis, S. E. (2003). Electrospray evaporation and deposition. *J. Aeros. Sci., 34,* 815-836.

Yang, W., Lojewski, B., Wei, Y., & Deng, W. (2012). Interactions and deposition patterns of multi-plexed electrosprays. *J. Aerosol Sci., 46,* 20-33.

Zhao, L. & Adamiak, K. (2005). EHD flow in air produced by electric corona discharge in pin–plate configuration. *J. Electrostat., 63,* 337-350.

FIGURE CAPTIONS

Fig. 1. Schematic diagram of the 2D axisymmetric computational domain for the gas flow, including boundary conditions.

Fig. 2. Numerical scheme for two-way coupling.

Fig. 3. Reactive drag force computed along the axis for different kernel widths.

Fig. 4. Spray snapshots projected on *rz* plane for (a) simulation with moving air, including the stream-lines of the induced air flow, and (b) simulation with still air. The circles diameters are proportional to the actual droplet diameters.

Fig. 5. Air velocity at various axial positions: (a) axial component, (b) radial component.

Fig. 6. Numerical and experimental values of axial velocities along the centerline for air and droplets.

Fig. 7. Average electrical forces, drag forces, and inertia sensed by the droplets along the centerline. Secondary abscissa shows the droplet Lagrangian time based on the droplet axial velocity given in Fig. 6.

Fig. 8. Radial profiles at z =1.2 cm of (a) droplet number density, and of (b) droplet diameter.

Fig. 9. Comparison of mass flux assuming still or moving air at (a) z = 1.2 cm and (b) z = 3.0 cm.